

Article

Performance Comparisons of Broadband Power Line Communication Technologies

Young Mo Chung 

Department of Electronics and Information Engineering, Hansung University, Seoul 02876, Korea; ymchung@hansung.ac.kr; Tel.: +82-2-760-4342

Received: 5 April 2020; Accepted: 6 May 2020 ; Published: 9 May 2020



Abstract: Broadband power line communication (PLC) is used as a communication technique for advanced metering infrastructure (AMI) in Korea. High-speed (HS) PLC specified in ISO/IEC12139-1 and HomePlug Green PHY (HPGP) are deployed for remote metering. Recently, internet of things (IoT) PLC has been proposed for reliable communications on harsh power line channels. In this paper, the physical layer performance of IoT PLC, HPGP, and HS PLC is evaluated and compared. Three aspects of the performance are evaluated: the bit rate, power spectrum, and bit error rate (BER). An expression for the bit rate for IoT PLC and HPGP is derived while taking the padding bits and number of tones in use into consideration. The power spectrum is obtained through computer simulations. For the BER performance comparisons, the upper bound of the BER for each PLC standard is evaluated through computer simulations.

Keywords: advanced metering infrastructure; power line communication; IoT PLC; HPGP; ISO/IEC 12139-1; HS PLC; bit error rate

1. Introduction

In a smart grid, the advanced metering infrastructure (AMI) is responsible for collecting data from consumer utilities and giving commands to them. AMI consists of smart meters, communication networks, and data managing systems [1,2]. An important challenge in building an AMI is choosing a cost-effective communication network [2–4]. As a field communication method for AMI, power line communication (PLC) or wireless communication can be considered. PLC deploys a pre-existent transmission medium, represented by the wires where the communication nodes are connected, so deployment and operating costs can be low.

PLC technologies can be classified into narrowband and broadband PLC according to the frequency bandwidth used. Narrowband PLC generally provides low data rates due to the narrow bandwidth of 3–500 kHz. To overcome the limitations of low rates and accommodate various service demands for utilities, powerline intelligent metering evolution (PRIME) and G3-PLC based on the orthogonal frequency division multiplexing technology were introduced [5]. These narrowband PLC technologies have been deployed for communication methods for AMI in European countries [5]. Broadband PLC uses a wide frequency bandwidth of 2–30 MHz. ITU-T G.hn, IEEE 1901, and ISO/IEC12139-1 [2,6] have been established as standards for broadband PLC. The HomePlug Powerline Alliance has also developed the HomePlug Green PHY (HPGP) standard for broadband PLC technology [7].

In Korea, most low-voltage customers are powered by pole-mounted transformers, and, on average, dozens of customers are connected to the transformer. The Korea Electric Power Corporation (KEPCO), a Korean power company, uses the ISO/IEC12139-1 standard PLC as an AMI field communication method in downtown residential areas [2]. The method is also referred to as high-speed (HS) PLC or Korean Industrial Standards (KS) PLC. HPGP is also being used in downtown areas. KEPCO plans to build AMI networks for 22.50 million low-voltage customers by 2020 [2,8].

In addition, several new services such as load profile (LP) metering and time-of-use (TOU) pricing are planned nationwide using AMI networks. To provide these services properly, more reliable communication is required. Recently, a new broadband PLC technology called IoT PLC [9] has been proposed for robust communication on power line channels. IoT PLC has several features for reliable communication. For example, it provides robustness to intersymbol interference (ISI) using orthogonal frequency division multiplexing (OFDM) with a longer guard interval than other methods, and convolutional turbo code (CTC) is used for forward error correction (FEC). In addition, it has a wide selectable range of repetitions from 1 to 15 for the coded bits, providing flexible transmission modes depending on the channel conditions. Currently, IoT PLC is being tested for deployment in Korea. One of three PLC technologies will be chosen for AMI through a performance competition: HS PLC, HPGP, or IoT PLC. Therefore, it is important to evaluate and compare the performance of these PLC technologies.

A PLC signal received through a power line is distorted due to the multipath propagation. Several broadband PLC channel models are available in [10,11]. One channel model is based on the transmission line (TM) theory and is suitable for the specified PLC network topology [12–16]. This model is known to have a realistic description of in-home power line topology [17]. Another channel model is obtained by matching the parametric multipath model of the channel frequency response with real data obtained from measurements [18]. This model represents the PLC channel as a finite sum of delayed echoes with different amplitudes [17]. In this paper, a broadband channel model in [18] is used for simulation and performance comparison. It is readily applied to an outdoor power line environment with obtained parameters in [18].

In addition, PLC signals are also corrupted by noise added by the power line channel. The noise is modeled as background noise added by impulsive noise [10,19–22]. The performance of the OFDM transmission scheme for PLC applications was investigated with the channel model in the presence of noise [22,23]. Studies on narrowband PLC standards such as G3-PLC and PRIME were conducted in [24, 25]. When it comes to performance comparisons of PLC standards, a few results have been reported. For narrowband PLC technologies, the performances of the physical layers of G3-PLC and PRIME were compared on a frequency-selective channel with additive white Gaussian noise (AWGN) [26]. In [27], performance comparisons were conducted with different noise environments. Physical layers of narrowband PLC including IEEE1901.2 were compared under AWGN and narrowband interferer in [28]. Recently, Llano et al. [5] compared the performances of the latest versions of the standards including PRIME 1.4 with that of G3-PLC coherent mode. The comparisons were made through the test metrics defined by the European Telecommunications Standards Institute (ETSI) in the presence of standard and controlled noise patterns. Unlike the physical layer of the narrowband PLC standards, studies are not widely conducted on the physical layer of broadband PLC standards. Especially, results of performance comparisons of broadband PLC standards such as HPGP and HS PLC have not been reported yet.

In this paper, studies on the performance evaluation of the IoT PLC as well as HPGP and HS PLC are conducted. The performances are evaluated in three aspects of the physical layer: the bit rate, power spectrum, and bit error rate (BER). The bit rates of the PLC are obtained with mathematical formulas. The power spectrum is obtained with a PLC signal generated by the computer in MATLAB codes. These two evaluations are relatively easy and simple compared to the BER evaluation. For the BER comparison, we obtain the upper bound of the performance for each standard. The BER performance depends on the transmitted signal specified in the standard and the receiver architecture. However, the receiver architecture is not specified in the standard. Therefore, it is assumed that each PLC receiver achieves the best performance possible. The equalizer in each receiver has a one-tap filter and is assumed to have a perfect channel estimation. In this context, impulsive noise is not included since our purpose is to obtain the upper performance bound for each PLC. For background noise, colored noise is known to reflect the noise of the PLC environment better. However, AWGN is also

considered useful when comparing the upper performance bound of the PLC. Through computer simulations, the upper bound of the performance of each PLC standard is evaluated and compared.

2. Structures of PLC

2.1. IoT PLC

The structure of an IoT PLC transmitter is shown in Figure 1 [9]. Two information subblocks A and B with N bits are provided to the CTC encoder. IoT PLC uses two values for N . For the data frame (DF), which is used for data transmission, N is 1440. The control frame (CF) or Mini DF uses a shorter frame length. For these frames, N is 48.

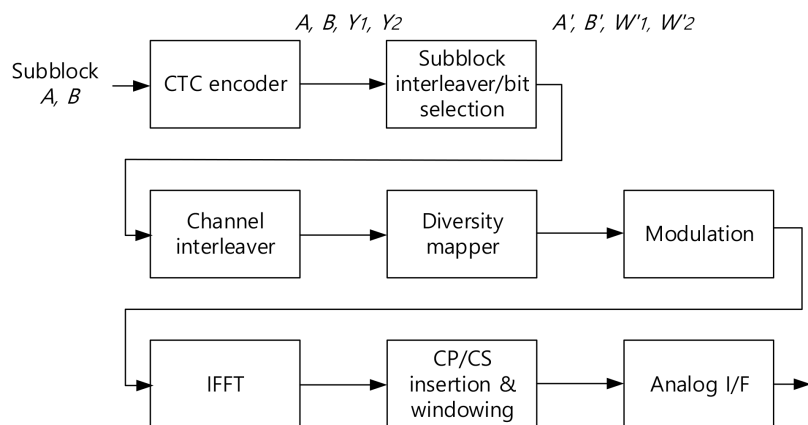


Figure 1. Block diagram of IoT PLC.

2.1.1. CTC Encoder

Figure 2 shows block diagram of the CTC encoder [9,29]. The CTC consists of two constituent encoders and a CTC interleaver as shown in Figure 2a. A double binary circular recursive systematic convolutional (RSC) encoder with a constraint length of 4 is used for the constituent encoder. Figure 2b shows the constituent encoder. When blocks A and B are encoded, a parity bit block Y_1 is generated. The inputs are then interleaved by the CTC interleaver, and the interleaved bits are encoded again by the constituent encoder, generating a parity block Y_2 . Y_1 and Y_2 each have N bits. The CTC interleaver shuffles the bit order in such a way that the bits are spread as evenly as possible. The outputs of the CTC encoder are A , B , Y_1 , and Y_2 , resulting in $4N$ output bits. For the initial state of the encoder, the start and end states are set to be the same, which is known as tail biting encoding and can improve the decoding performance without adding trailing bits at the encoder [30]. The CTC encoder generates $4N$ bits with a $2N$ bit input, resulting in a code rate of $1/2$.

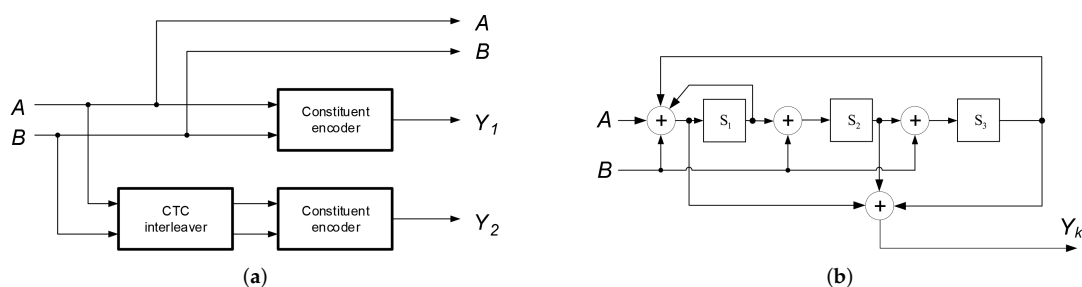


Figure 2. Block diagram of CTC encoder: (a) CTC encoder; and (b) constituent encoder.

2.1.2. Interleavers

Subblocks A , B , Y_1 , and Y_2 have their own subblock interleavers, which shuffle input bits within each subblock. The interleaver disperses corrupted bits in succession, thus burst bit errors are changed to random errors. The interleaved subblocks for A , B , Y_1 , and Y_2 are denoted as A' , B' , Y'_1 , and Y'_2 , respectively. Since turbo code works best for the random errors [31,32], the more dispersion there is, the better the interleaver. The bit selection block next to the subblock interleaver rearranges Y_1 and Y_2 once again: bits in Y'_1 are allocated to the odd positions in the output, and bits in Y'_2 are allocated to the even positions. The outputs of the bit selection block for parity blocks Y'_1 and Y'_2 are denoted as W'_1 and W'_2 .

Figure 3 shows the subblock interleaver and bit selection test inputs and their outputs for $N = 1440$ as an example. For visualization, integer numbers instead of binary numbers are assigned to subblock inputs. The subblock A has linearly increasing positive numbers, while B has decreasing negative numbers. In the same way, Y_1 and Y_2 are assigned but with larger and smaller slopes than A and B , respectively. The horizontal axis represents the sequence position and the vertical axis the value. The shuffled subblock A' has only positive values, which means that A is interleaved within the subblock. This also applies to subblock B . However, for the subblocks Y_1 and Y_2 , the outputs have both positive and negative values, which means that they are mixed together.

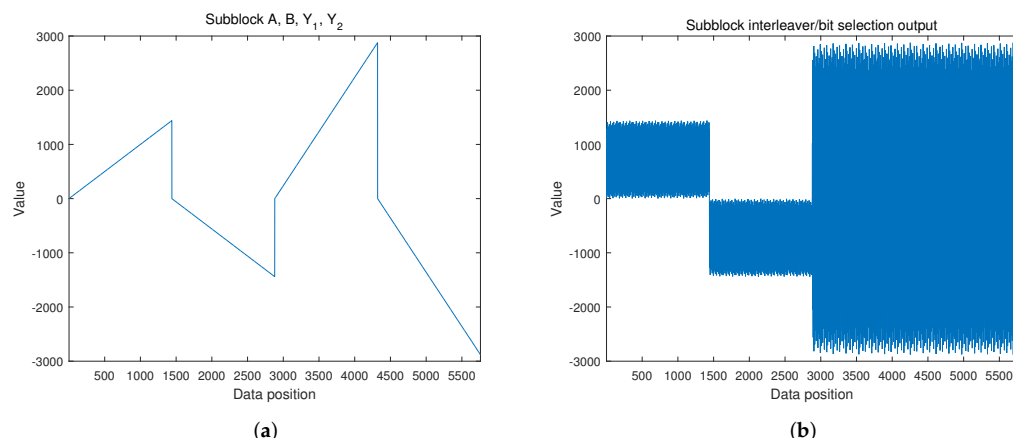


Figure 3. Subblock interleaver and bit selection block: (a) test input; and (b) output.

The channel interleaver further rearranges the input stream to improve the error correction capability of the CTC encoder by changing burst errors to random errors. Note that the channel interleaver works for all input data instead of subblocks. All bits from the four subblocks are successively written to a channel interleaving matrix in columns, and the bits of the matrix are read in rows. Row-by-row readings are done not continuously, but at regular intervals to separate the input bits as much as possible. The interleaver matrix has sizes of 720×8 for $N = 1440$ and 24×8 for $N = 48$.

Figure 4 shows the channel interleaver test input and corresponding output for $N = 1440$. For visualization, integer numbers instead of binary numbers are assigned for the inputs. The input has linearly increasing positive numbers. The horizontal axis represents the data sequence position and the vertical axis represents the value. From the channel interleaver output stream, the input data are dispersed evenly, thus the adjacent bits for each bit are placed as far apart as possible.

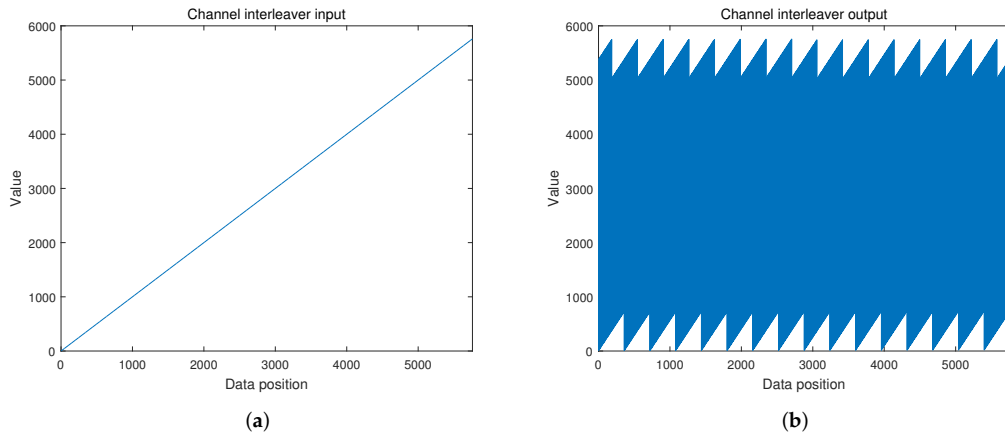


Figure 4. Channel interleaver: (a) test input; and (b) output.

2.1.3. Diversity Mapper

The diversity mapper copies the input bits by a specified number of times. The number of copies is specified by parameter DV_n . Users can set the values of DV_n from 1 to 15. OFDM is used in the transmission technique. The copied bits are placed at different frequencies and times of OFDM symbols. This gives the input bit frequency and time diversity, providing robustness against frequency-selective and time-varying distortions in the PLC channel.

An OFDM symbol has a number of usable subcarriers, or tones, denoted as N_{tone} . Each tone can transmit N_{bpt} bits, depending on the modulation scheme used. When quadrature phase shift keying (QPSK) is used for modulation, $N_{bpt} = 2$. The number of diversity mapper input bits is $4N$ and the number of copies is DV_n . Then, the number of bits to be transmitted is $4N \times DV_n$ bits and an OFDM symbol can carry up to $N_{tone} \times N_{bpt}$ bits. Note that $4N \times DV_n$ is not always an integer multiples of $N_{tone} \times N_{bpt}$. The number of tones in use is denoted as N'_{tone} , and extra padding bits are introduced. The padding bits are added at the end of the diversity mapper input bits and copied together. The padding bits are filled with the preceding bits of the diversity mapper inputs. The number of padding bits is denoted as N_{pad} , and the number of required OFDM symbols is denoted as N_{sym} . Then, the following equation should hold for all integer-valued variables.

$$(4N + N_{pad}) \times DV_n = (N'_{tone} \times N_{bpt}) \times N_{sym}. \quad (1)$$

A method is described to find N'_{tone} , N_{pad} , and N_{sym} when integer values are given for N , DV_n , N_{tone} , and N_{bpt} [9]. Figure 5a shows N_{pad} and N'_{tone} according to DV_n when $N = 1440$, $N_{tone} = 800$, and $N_{bpt} = 2$. It is observed that N_{pad} varies from 0 to 640 depending on DV_n . However, the variation of N'_{tone} is very small.

Next, it is necessary to place the copied bits far apart in the frequency bands of OFDM symbols to fully exploit frequency diversity. The detailed frequency mapping algorithm is described in [9]. Figure 5b shows the frequency allocation result for the copied bits when $DV_n = 15$ as an example. When $DV_n = 15$, $N'_{tone} = 795$, $N_{bpt} = 2$, and $N = 1440$, 55 OFDM symbols are required for the entire data transmission. The horizontal axis represents time, more specifically, the OFDM symbol sequence number. The vertical axis represents frequency, i.e., the subcarrier number of the OFDM symbol. It is noted that 15 copies of a bit are located at different frequencies and times with a considerable distance, providing robustness against distortions in both the frequency and time domain.

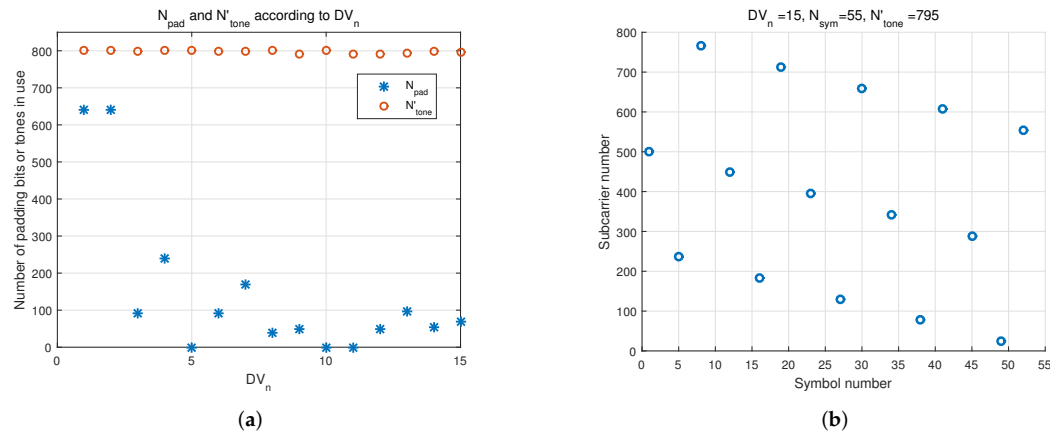


Figure 5. Diversity mapper: (a) number of padding bits and tones in use; and (b) locations of the copied bits.

2.1.4. Modulation, IFFT, CP/CS Insertion, and Windowing

For modulations, both coherent and noncoherent schemes are used. For the coherent scheme, QPSK or 16-ary quadrature amplitude modulation (16QAM) is used. 16QAM has 16 signal space points, thus 4 bits can be conveyed by one 16QAM symbol. For a noncoherent scheme, $\pi/4$ -differential phase shift keying ($\pi/4$ -DQPSK) is used. With the selected modulation technique, the binary values from the diversity mapper are converted to complex symbols.

OFDM symbols are produced by an inverse fast Fourier transform (IFFT). By modulation, 1280 complex symbols and their complex conjugates are converted to a real-valued OFDM symbol through a 2560-point IFFT. OFDM symbols have a cyclic prefix (CP) and a cyclic suffix (CS) before and after each symbol, respectively. The CP and CS make symbols resistant to intersymbol interference (ISI). For the CP and CS, 944 and 336 samples are used, respectively. Figure 6 shows an OFDM symbol structure.

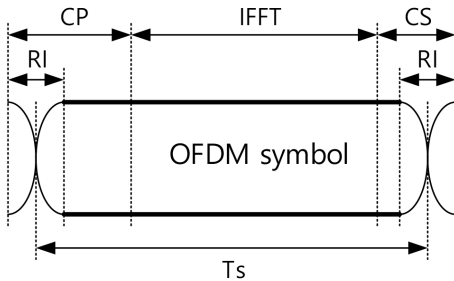


Figure 6. OFDM symbol.

At both ends of the symbol, samples are shaped to have a good power spectrum, and the interval is referred to as roll-off interval (RI), as shown in Figure 6. A detailed description of values in Figure 6 is given in [9]. For the pulse shaping, raised-cosine windowing is used. For the RI, 320 samples are used. The RI is overlapped and added to the adjacent RIs. The sampling frequency f_s is 62.5 MHz. There are 3520 samples in an OFDM symbol period T_s , which corresponds to 56.32 μ s. Finally, the OFDM symbols go to the analog interface (I/F) block, and the output signal is transmitted to the receiver through the channel.

2.2. HPGP

A detailed description of HPGP is found in [7]. In this section, a brief description for the physical layer of HPGP is given for the sake of completeness. In Figure 7, a block diagram for the physical layer of HPGP is shown. The information bits are provided in physical block (PB) units. For payload symbols, PB136 and 520 are used, which have 136 and 520 bytes in the block, respectively. For FEC, a

rate 1/2 turbo convolutional code is used and a double binary RSC encoder with a constraint length of 4 is used for the constituent encoder. The turbo convolutional code of HPGP is similar to the CTC of IoT PLC. However, the generator and feedback polynomials of the constituent coder are different. At PB136, there are 1088 input bits. Thus, the size of each input block N is 544. For PB520, N is 2080.

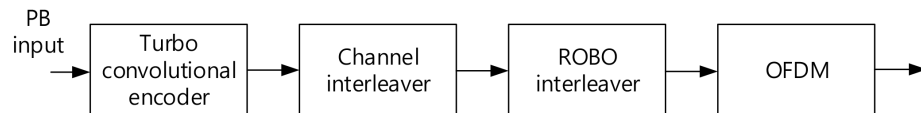


Figure 7. Block diagram of HPGP.

The encoded bits go to the channel interleaver. The channel interleaver uses an interleaver matrix. In HPGP, information blocks and parity blocks are interleaved separately, unlike in IoT PLC. Two 1040×4 matrices are used for PB520, while two 272×4 matrices are used for PB136. The row-wise 4-bit output of each matrix is shuffled once more through subblock switching. The robust OFDM (ROBO) interleaver copies the input bits for the output. The function is essentially the same as the diversity mapper of IoT PLC. HPGP has three ROBO modes: standard (STD), high speed (HS), and mini (MINI). The number of copies for the input bits for STD, HS, and MINI modes is 4, 2, and 5, respectively. STD and HS modes use PB520, whereas MINI mode uses PB136.

HPGP uses OFDM for the transmission technique. For modulation, only coherent QPSK is used. The number of IFFT points is 3072. CP is also used to mitigate the effect of ISI. However, CS is not used in HPGP. There are 372 samples of RI at both ends of the symbol. For the pulse shaping, raised-cosine windowing is used. The sampling frequency f_s is 75 MHz. It is noted that the length of the guard interval (GI) depends on the ROBO modes. The length of GI is the length of CP minus RI. In STD and HS modes, 417 samples are assigned to the GI, whereas 567 samples are assigned to the MINI mode. The OFDM symbol period is $(3072 + GI)$ samples long, which corresponds to $(40.96 + \tau)$ μ s. For STD and HS modes, $\tau = 5.56 \mu$ s, whereas $\tau = 7.56 \mu$ s for MINI mode.

2.3. HS PLC

In this section, a brief description for the physical layer of HS PLC [6] is given. In Figure 8, a block diagram of the HS PLC physical layer is shown. The binary input is provided to the FEC block. For data frames, different FEC schemes are used according to three operating modes: NORMAL, diversity (DV), and extended diversity (EDV) mode. For NORMAL mode, a concatenated code with Reed–Solomon (RS) and convolutional code is used. The RS code uses a shortened code of (255, 239). The rate of the convolutional code is 1/2 or 3/4 and the constraint length is 7. For signal transmission in HS PLC, discrete multi-tone is used, which is essentially the same as OFDM. Thus, in this paper, it is called OFDM instead of DMT. A symbol block (SB) consists of 16 OFDM symbols. Encoding is performed by each SB unit. Then, the encoded bits of an SB are interleaved with an interleaving matrix of size $N_{BPS} \times 16$, where N_{BPS} represents the number of bits in an OFDM symbol. N_{BPS} depends on the modulation method, which is determined by the channel conditions. In NORMAL mode, encoded bits bypass the diversity mapper. For modulation, differential phase shift keying (DBPSK), DQPSK, or differential 8 phase shift keying (D8PSK) is used for each subcarrier of OFDM. The selection among the three modulations is made based on the channel condition. Information on the modulations selected for all the subcarriers is called a tone map (TM) and is transmitted to the communicating receivers.

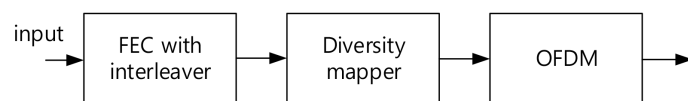


Figure 8. Block diagram of HS PLC.

In DV mode, (20, 12) RS code is used. An input block of 96 bits is encoded, and a 160-bit output block is generated. These output bits go to the diversity mapper directly, and are transmitted by 16

OFDM symbols. In an OFDM symbol, 124 subcarriers with DBPSK are used and 10 encoded bits are transmitted. Thus, each encoded bit is copied at least 12 times. DV mode is the most reliable communication mode in HS PLC. In the case of EDV mode, (56, 40) RS code is used. This encoder generates 448 bits with a 320-bit input block. These output bits go to the diversity mapper directly, and are transmitted by 16 OFDM symbols as in DV mode. In an OFDM symbol, 152 subcarriers with DBPSK are used, and 28 encoded bits are transmitted, resulting in five copies for each encoded bit.

The number of IFFT points for OFDM is 512. In HS PLC, CP is also used as in the other PLC technologies and 128 samples are assigned. At both ends of symbols, there are RIs of 16 samples. For the pulse shaping, raised-cosine windowing is used as in the other PLC technologies. The sampling frequency f_s is 50 MHz. The OFDM symbol period is 624 samples long, which corresponds to 12.48 μ s.

3. Bit Rate and Power Spectrum Comparisons

The operating modes and data protection methods of the PLC technologies are summarized in Table 1. HPGP and HS PLC each have three operating modes, and each mode has its own diversity number. However, IoT PLC has Mini DF and Normal DF, and Normal DF has 15 different diversity numbers, enabling very flexible operations. In Normal DF mode of IoT PLC, the diversity number is determined by the diversity field setting in the physical layer (PHY) header. The diversity number of 15 of IoT PLC is the largest of the three PLC technologies, and provides powerful error correcting capabilities.

CTC is known to have very strong error correcting capability against random errors. Thus, it is necessary to change burst errors that usually occur in the PLC channel into random ones. This is why IoT PLC and HPGP use interleavers for all modes. HS PLC uses an interleaver in NORMAL mode only. The size of N_{BPS} depends on the TM determined by the channel conditions. DV and EDV modes do not use an interleaver.

As mentioned above, IoT PLC and HPGP use a rate 1/2 CTC for FEC. However, their constituent encoders are different. HS PLC uses a concatenated code of RS and convolutional code or RS code alone depending on the operation mode. These codes have relatively weak error correction capabilities compared to CTC.

Table 1. Operation modes and data protection schemes.

Mode	IoT PLC			HPGP			HS PLC		
	Normal DF	Mini DF	STD	HS	MINI	NORMAL	EDV	DV	
DV_n	1–15	16	4	2	5	1	5	12	
Interleaver size	720×8	24×8	two of (1040 \times 4)	two of (1040 \times 4)	two of (272 \times 4)	$N_{BPS} \times 16$	-	-	
FEC	rate 1/2 CTC	rate 1/2 CTC	rate 1/2 CTC	rate 1/2 CTC	rate 1/2 CTC	(255,239) RS + rate 1/2 CC	(56,40) RS	(20,12) RS	

All three PLC technologies use the OFDM technique for transmission. The channel and OFDM parameters are summarized in Table 2. The frequency bands used for IoT PLC and HPGP are 2 to 28 MHz. However, HS PLC uses a narrower frequency bands. In these frequency bands, bands used by other wireless communications and regulated by emission laws can not be used. Therefore, the number of usable subcarriers is smaller than half of the IFFT size. The sampling frequency f_s and the IFFT size determine the subcarrier spacing. HPGP has the smallest subcarrier spacing, and HS PLC has the largest subcarrier spacing. The small value of the subcarrier spacing makes it easy to control the PLC signal spectrum where allowed and forbidden bands are closely located. The signal spectrum shape is also related to the RI value. The large RI value results in low out-of-band spectral components. IoT PLC has the largest RI value and HS PLC has the smallest RI.

Table 2. Channel and OFDM parameters.

	IoT PLC		HPGP			HS PLC		
Mode	Normal DF	Mini DF	STD	HS	MINI	NORMAL	EDV	DV
Freq. bands (MHz)	2–28	2–28	2–28	2–28	2–28	4–23	4–23	4–23
IFFT size	2560	2560	3072	3072	3072	512	512	512
Number of subcarriers in use	800	800	916	916	915	152	152	124
f_s (MHz)	62.5	62.5	75	75	75	50	50	50
Subcarrier spacing (kHz)	24.41	24.41	12.21	12.21	12.21	97.66	97.66	97.66
Symbol period (μs)	56.32	56.32	46.52	46.52	48.52	12.48	12.48	12.48
CP (μs)	15.10	15.10	10.52	10.52	12.52	2.56	2.56	2.56
CS (μs)	5.38	5.38	-	-	-	-	-	-
RI (μs)	5.12	5.12	4.96	4.96	4.96	0.32	0.32	0.32
Modulation	QPSK, 16QAM, $\pi/4$ -DQPSK	QPSK	QPSK	QPSK	QPSK	DBPSK, DQPSK, D8PSK	DBPSK	DBPSK

CP and CS increase the symbol period, and decrease the symbol rate. However, CP and CS serve to reduce the influence of the ISI caused by the channel. IoT PLC has the largest CP and CS value among the three PLC technologies. HS PLC has the smallest CP values. IoT PLC and HS PLC have the same CP and CS values regardless of the operation modes, whereas HPGP has different CP values depending on the operation modes. The MINI mode of HPGP has a larger CP value than the STD and HS modes.

For modulations, HPGP uses coherent QPSK in all three modes. Coherent QPSK is also used for Normal DF and Mini DF of IoT PLC. Normal DF also uses coherent 16QAM and noncoherent $\pi/4$ -DQPSK. HS PLC uses noncoherent modulation methods. In NORMAL mode, DBPSK, DQPSK, or D8PSK is used depending on the channel conditions. Information about the used subcarrier modulations is transmitted in the form of TM. D8PSK can transmit 3 bits per subcarrier, but it is more susceptible to noise than DBPSK and DQPSK. DV and EDV modes use DBPSK, which is the most robust against noise and distortions among the three differential modulations.

For IoT PLC, the transmission rate is given as follows.

$$R_{IoT} = \frac{1}{T_s} \times N'_{tone} \times N_{bpt} \times R_{FEC} \times \frac{1}{DV_n} \times \frac{4N}{4N + N_{pad}} (\text{bps}), \quad (2)$$

where T_s and R_{FEC} represent the symbol period and rate of the FEC, respectively. The results for the transmission rate are shown in Table 3. In IoT PLC, $R_{FEC} = 1/2$. The values of N'_{tone} and N_{pad} depend on N_{tone} and DV_n . Although N'_{tone} is not equal to N_{tone} , the difference between the two values is small. In addition, the number of padding bits, N_{pad} , is not large compared to $4N$. Thus, Equation (2) can be approximated as follows.

$$R = \frac{1}{T_s} \times N_{tone} \times N_{bpt} \times R_{FEC} \times \frac{1}{DV_n} (\text{bps}). \quad (3)$$

Note that the values of T_s , N_{tone} , N_{bpt} , and DV_n are found in the specifications. Thus, with Equation (3), the transmission rate can be easily obtained. In addition, Equation (3) can also be applied to obtain the transmission rate for HPGP and HS PLC.

The results for transmission rate obtained by Equation (2) at each DV_n are given Figure 9 when $N_{tone} = 800$ and $N = 1440$. In this figure, the results with Equation (3) are also provided for comparison. N_{bpt} can be 2 or 4 for IoT PLC. In Figure 9, the approximated results agree well with the results from Equation (2) except for the cases of small DV_n . Specifically, when $N_{bpt} = 2$ and $DV_n \geq 3$, the difference

due to the approximation is almost negligible. When $N_{bpt} = 4$ and $DV_n \geq 5$, the difference due to the approximation is also almost negligible.

Table 3. Transmission rate for IoT PLC (Mbps).

DV_n	1	2	3	4	5	6	7	8
Rate, $N_{bpt} = 2$	12.784	6.392	4.649	3.409	2.841	2.324	1.967	1.763
Rate, $N_{bpt} = 4$	25.568	12.784	8.523	6.392	5.682	4.649	3.934	3.409
DV_n	9	10	11	12	13	14	15	Mini DF
Rate, $N_{bpt} = 2$	1.550	1.421	1.278	1.162	1.065	1.003	0.930	0.852
Rate, $N_{bpt} = 4$	3.008	2.841	2.557	2.324	2.131	1.967	1.826	-

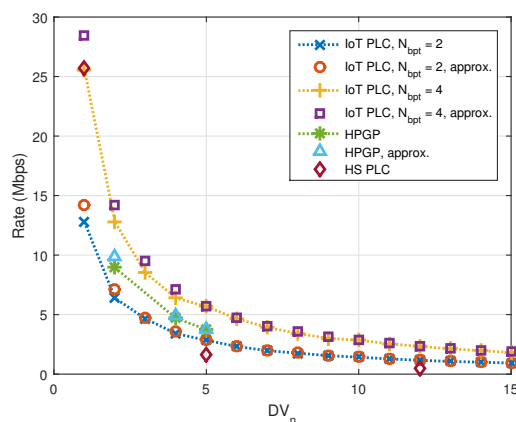


Figure 9. Transmission rate of IoT PLC according to diversity numbers.

For HPGP, $N_{bpt} = 2$ and $R_{FEC} = 1/2$, regardless of the operating modes. The symbol period T_s and the number of subcarriers in use N_{tone} are shown in Table 2. The diversity number is shown in Table 1. Padding bits are also used in HPGP. Using Equation (2), the transmission rates are obtained and are shown in Table 4. The approximate transmission rates using Equation (3) are also obtained and shown in parentheses. The results of the transmission rates are shown in Figure 9 for comparison.

Table 4. Transmission rate for HPGP and HS PLC (Mbps).

Mode	HPGP			HS PLC		
	STD	HS	MINI	NORMAL	EDV	DV
Rate	4.707 (4.923)	8.942 (9.845)	3.737 (3.772)	≤ 25.684	1.603	0.481

In the NORMAL mode of HS PLC, the transmission rate varies according to the TM and the rate of the FEC, which can be set by the software or operator. We choose the maximum value of R_{FEC} for convenience, which is equal to $(239/255) \times (3/4)$. In addition, N_{bpt} changes with the modulation method determined by the TM. Likewise, we choose the maximum value of 3 for N_{bpt} . Thus, the transmission rate obtained for the NORMAL mode is the maximum that the mode can achieve.

For EDV and DV modes, 40 information bytes and 12 bytes are transmitted by 16 OFDM symbols, respectively. Using the values in Tables 1 and 2, the transmission rates are obtained by Equation (2). The transmission rates for HS PLC are shown in Table 4. The transmission rate for NORMAL mode, 25.684 Mbps, is the maximum rate, when assuming that D8PSK is used for each subcarrier, and the rate 3/4 CC is employed for the FEC. When the rate 1/2 CC is used for the FEC, the transmission rate decreases to 17.123 Mbps. For the modes of DV and EDV, the values are the actual transmission rates of the physical layer. These transmission rates for HS PLC are also shown in Figure 9.

There are several methods to numerically estimate the power spectrum or power spectral density, such as periodograms and Welch's method. Welch's method is known to reduce the noise in the

estimated power spectra which is noticeable in a periodogram [33]. We estimate the power spectrum of the transmitted PLC signals by Welch's method.

The number of samples used to obtain the spectrum is about 1 million. Figure 10a shows the power spectrum of the IoT PLC signal. The horizontal axis ranges from 0 to half of the sampling frequency. The signal is designed to occupy the frequency band of 2–28 MHz. However, in the band, there are forbidden ranges due to the use of wireless communication such as short-wave radio and amateur radio. As in other countries around the world, the radiation levels for each frequency band are strictly regulated by law in Korea. In Figure 10a, the notches are located in the forbidden bands and are very deep. The power at band edges is about 70 dB lower.

Figure 10b,c shows the spectrum results for HPGP and HS PLC, respectively. The frequency range is from 0 to $f_s/2$, which corresponds to 37.5 and 25 MHz for HPGP and HS PLC, respectively. The frequency bands for HPGP and HS PLC are 2–28 and 4–24 MHz, respectively. In the computer experiment, the subcarrier masks in the standards [6,7,9] are applied, and the power of the transmitted signals for the three PLC technologies is made to be equal. Since the bandwidth of HS PLC is narrower than the others, the power spectrum level is higher. The spectrum notches in HS PLC is very shallow compared to those of the others. The notches are only about 20–25 dB deep because the RI value of HS PLC is short. Since the power at the band edges is observed only about 30 dB lower, an additional analog filter is needed to control the sidelobe power. In HPGP, the notch depth is about 30–40 dB and the power at band edges is about 40 dB lower. Thus, HPGP has better power spectrum properties than HS PLC in terms of the notch depth and out-of-band power. IoT PLC has better spectral properties than HPGP since IoT PLC has deeper notches and lower out-of-band power than HPGP.

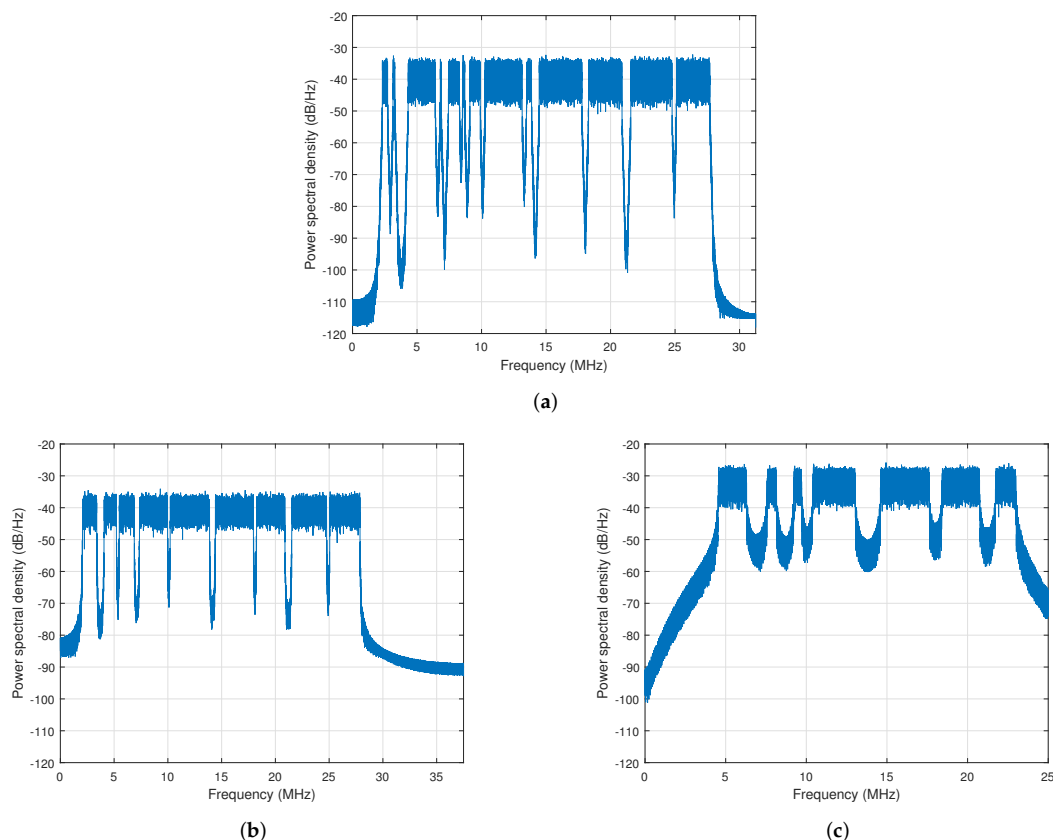


Figure 10. Power spectrum: (a) IoT PLC; (b) HPGP; and (c) HS PLC.

4. BER Comparisons and Discussion

4.1. Computer Simulation Blocks

The communication reliability for the PLC physical layer is investigated in terms of BER. Figure 11 shows the computer simulation block diagram for BER measurement. Randomly generated bits are processed at the transmitter, and the output OFDM signal of the transmitter enters the PLC channel. The channel output corrupted by noise is input to the receiver. The receiver specifications for the three PLC technologies are not given in the standards. Thus, the algorithm used for each PLC receiver is designed to achieve the best performance possible. In this context, impulsive noise is not included since our purpose is to obtain the upper performance bound for each PLC. For background noise, colored noise is known to reflect the noise of the PLC environment better. However, AWGN is also considered useful when comparing the upper performance bound of the PLC technologies. Thus, for the noise, AWGN is used in the simulation. The performance comparisons are based on the upper limit of the performance that each PLC specification can achieve.

The IoT PLC receiver in Figure 11 consists of several functional blocks. In this paper, it is assumed that symbol and carrier synchronization between the transmitter and the receiver is perfect. That is, there is no timing error and no carrier frequency error at the receiver. CP and CS are removed from the received signal, which is then converted to the frequency domain by FFT. There are pilot symbols or pilot carriers in the transmitted signal to help channel estimation. Algorithms to estimate the channel response from the pilot tones have been described, and each algorithm has pros and cons [34]. Since our goal is to evaluate the upper limit of the BER performance, we assume a perfect channel and signal-to-noise ratio (SNR) estimation. The channel response is used to equalize each distorted subcarrier signal by a frequency domain one-tap equalizer using the minimum mean square error (MMSE) algorithm.

The equalized subcarrier signals are demodulated. The demodulator produces soft decision values since CTC decoding uses soft decision inputs. The demodulated in-phase or quadrature components are combined by the diversity demapper. The combined values are sent to the channel deinterleaver and subblock deinterleaver, which function as an inverse channel interleaver and subblock deinterleaver, respectively.

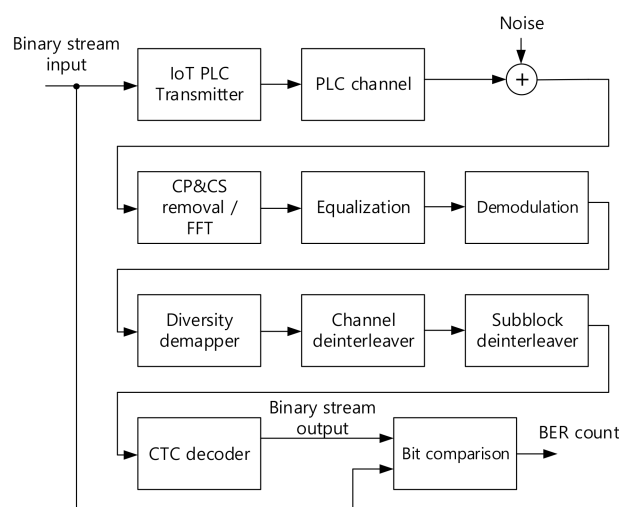


Figure 11. Simulation block diagram for BER measurements.

For CTC decoding, several methods are described in the literature [35–37]. Maximum a posteriori (MAP) or log-MAP, which is the log-domain implementation of the MAP, is the optimal decoding algorithm. Log-MAP provides less computational burden than MAP, but the complexity is still high. The max-log-MAP algorithm with a correction term has viable complexity and provides equivalent performance to the log-MAP. Thus, the max-log-MAP with a correction term is used for CTC decoding.

This algorithm is also used when the performance of HPGP is evaluated. Finally, the decoded bit stream is compared to the input bit stream and the BER is computed.

4.2. Channel Model

The broadband channel model in [18] is described briefly. The frequency response of the channel is as follows.

$$H(f) = \sum_{k=1}^K g_k \cdot A(f, d_k) \cdot e^{-j2\pi f(d_k/v_p)}, \quad (4)$$

where g_k is a weighting factor and $A(f, d_k)$ is an attenuation. The last portion $e^{-j2\pi f(d_k/v_p)}$ represents delay, where d_k and v_p are the length of the k th path and the propagation speed on the transmission line, respectively. K represents the number of signal paths between the transmitter and receiver. The attenuation $A(f, d_k)$ and the parameters g_k and d_k are obtained from field measurements.

When a power line has one tap and the number of signal paths is 4, the attenuation and the parameters are obtained in [18]. The magnitude response of this model with the attenuation and parameters is shown in Figure 12a. This model covers all substantial effects of the transfer characteristics in the frequency range from 500 kHz to 20 MHz. However, observing that the attenuation decreases as the frequency increase in the range above 20 MHz, it is believed that this model can be used up to 28 MHz without loss of generality.

For the simulation, the frequency response is cut to the range of half the sampling frequency of IoT PLC and sampled with the frequency resolution of subcarrier spacing. Then, the discrete impulse response obtained from the sampled channel frequency response is convolved with the sampled IoT PLC signal to produce the channel output. This method also applies to HPGP and HS PLC. Since their sampling frequency and subcarrier spacing are different, each discrete channel impulse response is obtained accordingly. The discrete impulse response for IoT PLC is shown in Figure 12b as an example.

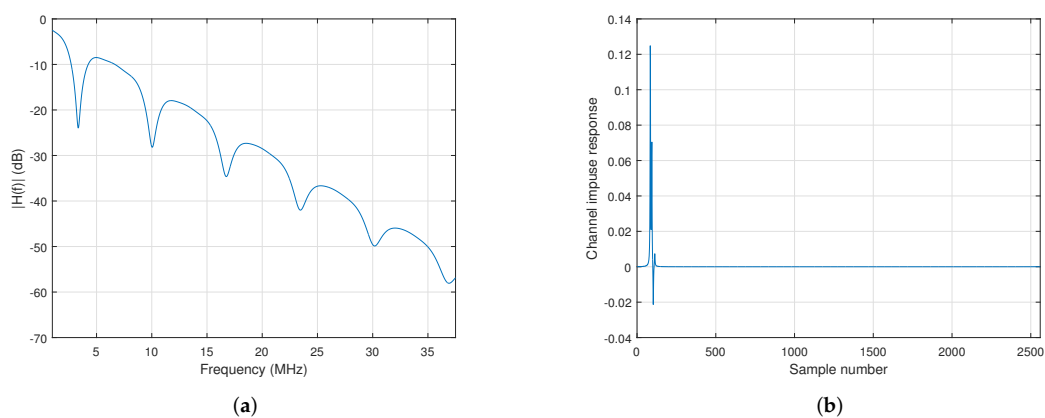


Figure 12. PLC channel: (a) magnitude frequency response of the channel; and (b) channel impulse response for IoT PLC.

4.3. Simulation Results and Discussion

The CTC decoder decodes the input block by an iterative algorithm. The CTC decoder has two soft-input soft-output (SISO) decoders, which compute a posteriori log-likelihood ratio (LLR) for information bits. With soft-decision inputs and a priori LLR of information bits, a SISO decoder also produces an extrinsic information. The extrinsic information is provided to the other SISO decoder as an updated a priori LLR. This process is done iteratively. As the iteration continues, a posteriori LLR values become more reliable with the updated a priori LLRs. Detailed descriptions of the iterative decoding algorithm are given in [35–37]. After each iteration, errors in the decoded bits are reduced. The BER results for IoT PLC with QPSK modulation are shown in Figure 13. The number of information

bits for subblocks A and B used in the simulation is about 10^6 . The diversity number DV_n of IoT PLC is 1–15. The SNR in dB is defined as $10\log_{10}(S_p/N_p)$, where S_p and N_p are the signal power and noise power at the receiver, respectively. In Figure 13, the results for diversity numbers of 3 and 15 are shown as examples. In the figures, the BER value decreases as the number of iterations increases. In the second iteration, the BER performance is greatly improved. However, the BER improvement becomes saturated when the iterations are large. The difference between the BER results at Iterations 6 and 8 is very small. In addition, the BER drops rapidly when $\text{SNR} \geq -5$ dB and $DV_n = 3$. However, when DV_n increases to 15, the rapid fall of the BER begins at a much lower SNR of -13.5 dB. When $DV_n = 3$ and 15, the required SNR to obtain 10^{-3} for the BER is -3.3 dB and -12.8 dB at six iterations, respectively.

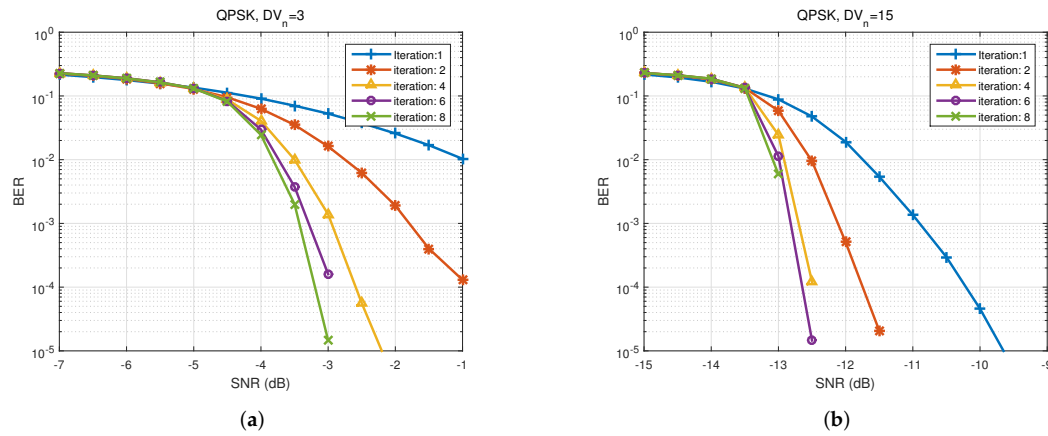


Figure 13. BER results for IoT PLC with QPSK modulation: (a) $DV_n = 3$; and (b) $DV_n = 15$.

The BER results for IoT PLC with 16QAM modulation are shown in Figure 14. The shape of this figure is similar to that of Figure 13. However, the beginning SNR for a rapid BER fall is very large. For example, the BER drops rapidly when $\text{SNR} \geq 5$ dB and $DV_n = 3$. When $DV_n = 15$, the BER shows rapid fall at $\text{SNR} \geq -5.5$ dB. In addition, as DV_n increases, the slopes of the falling portion of the curves are steeper, which is also seen in Figure 13.

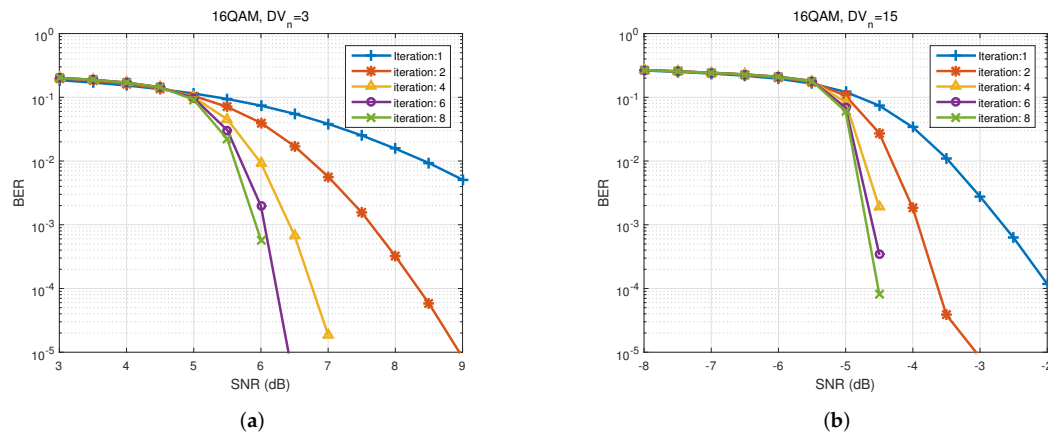


Figure 14. BER results for IoT PLC with 16QAM modulation: (a) $DV_n = 3$; and (b) $DV_n = 15$.

The BER results for IoT PLC with $\pi/4$ -DQPSK modulation are shown in Figure 15. For $\pi/4$ -DQPSK mode, noncoherent detection is used. The channel equalizer is not applied for this mode. The differential detection is performed with symbols adjacent in time in the same subchannel. On static or slowly changing channels, distortions caused by the channel can be compensated with differential detection. When $DV_n = 3$, an irreducible error floor is observed. The subchannel located at the deep notch of the channel has unrecoverable bit errors. If the diversity number is not large, the bit

copies are not spread enough to be corrected, which results in error floor. When $DV_n = 15$, the error floor is not present and the BER decreases rapidly as the SNR increases owing to the rich diversity. With the channel used in the simulation, the error floor is not observed in the range down to 10^{-5} when $DV_n \geq 4$.

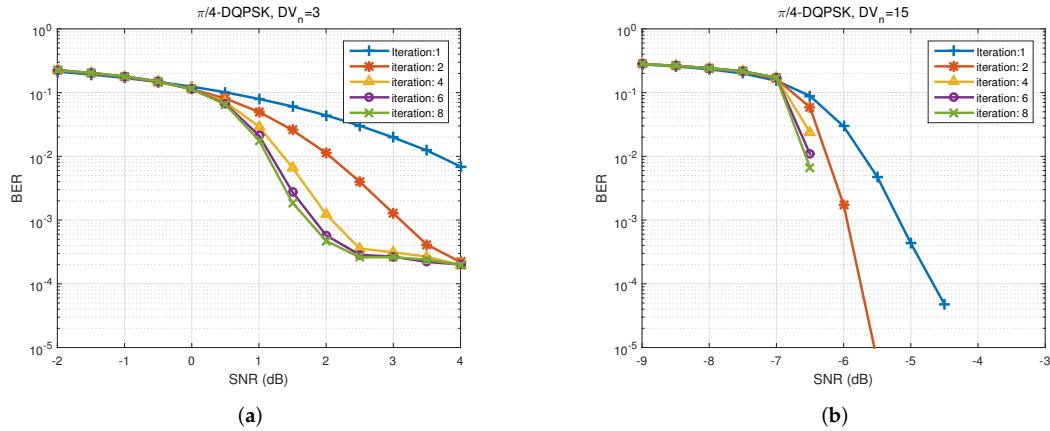


Figure 15. BER results for IoT PLC with $\pi/4$ -DQPSK modulation: (a) $DV_n = 3$; and (b) $DV_n = 15$.

Next, the BER results for Mini DF are shown in Figure 16. In Mini DF mode, QPSK modulation is used and the block size is $N = 48$. Since the block size is smaller than that of DF, the BER shows a relatively slow decrease with increasing SNR, which is commonly observed in systems with CTC of small processing blocks. However, for Mini DF mode with many copies of coded bits (16 copies), the BER begins to fall at a low SNR of -14 dB. The required SNR to obtain 10^{-3} for the BER is -11.7 dB at six iterations.

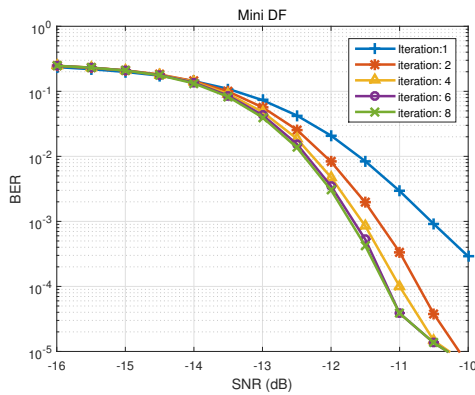


Figure 16. BER results for Mini DF.

Next, the performance change according to the diversity number at each modulation is investigated. The BER results for the whole values of DV_n are shown in Figure 17, where the iteration number is set to 6. The BER performance improves as DV_n increases. In Figure 17a, to obtain a BER of 10^{-3} in QPSK mode, an SNR of 0.3 dB is required with $DV_n = 2$ and an SNR of -3.3 dB with $DV_n = 3$. Thus, an SNR improvement of 3.6 dB is obtained owing to the diversity number increasing from 2 to 3. However, the performance improvement obtained from the diversity becomes small when the diversity number becomes large. For example, when the diversity number increases from 9 to 10, an SNR improvement of 0.4 dB is obtained. The other modulations, 16QAM and $\pi/4$ -DQPSK, show a similar trend.

Figure 17b shows the BER results for 16QAM mode. The BER hardly decrease even with a large SNR when $DV_n = 1$. However, when $DV_n \geq 2$, the BER decreases rapidly as the SNR increases. Without diversity, a bit may be not recovered even at a high SNR due to a deep notch in the channel,

but in the presence of diversity, copies of the bit can make the bit correctable. At $\text{BER}=10^{-3}$, an SNR improvement of 2.95 dB is obtained with a DV_n increase from 2 to 3. When DV_n increases from 9 to 10, an SNR improvement of 0.31 dB is observed at $\text{BER}=10^{-3}$. In Figure 17c, the BER results for $\pi/4$ -DQPSK mode are shown. Comparing the BER performance of $\pi/4$ -DQPSK mode with that of the other modes at every DV_n , the BER performance of $\pi/4$ -DQPSK is better than that of 16QAM but is worse than that of QPSK.

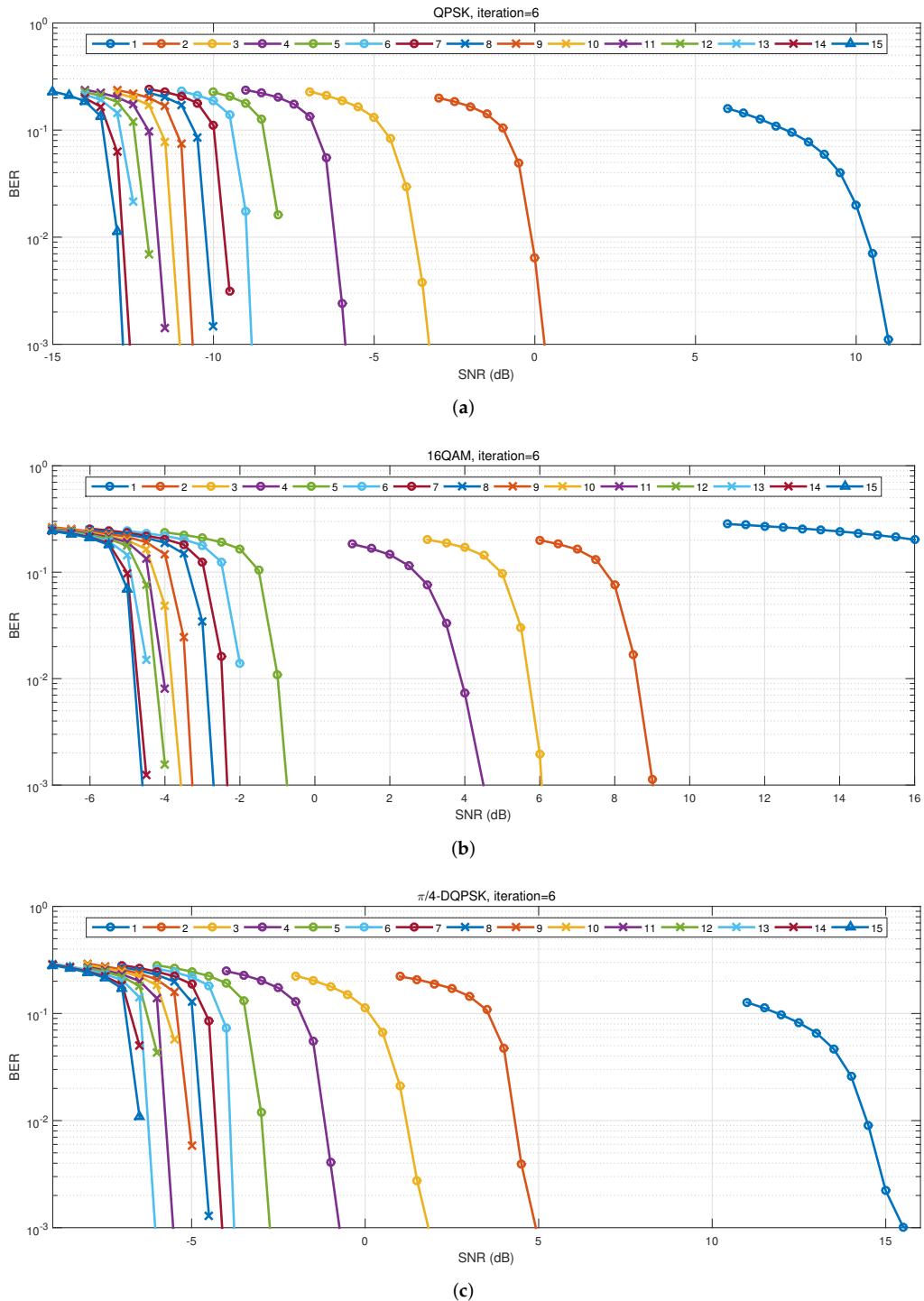


Figure 17. BER results of IoT PLC for the whole DV_n : (a) QPSK mode; (b) 16QAM mode; and (c) $\pi/4$ -DQPSK mode.

HPGP uses CTC for the FEC. Thus, iterative decoding is used as in IoT PLC. Figure 18 shows the BER results for HPGP. BER values are given at Iterations 2, 4, 6, and 8. As the iterations increase, the BER difference between iterations decreases. The block size for STD and HS modes is 2080, while the block size of MINI mode is 544. The falling slope of the BER curve in Figure 18a is less steep than those in the other modes, because the block size at the MINI mode is smaller. The STD mode makes four copies for the coded bits while HS makes two copies. Thus, the STD mode outperforms the HS mode in terms of the BER. At a BER of 10^{-3} , the STD mode requires an SNR of -5.7 dB while the HS mode requires 1.3 dB. The MINI mode has the most copies for the coded bits, but the BER performance at high SNR is not better than the STD mode because of the small input block size.

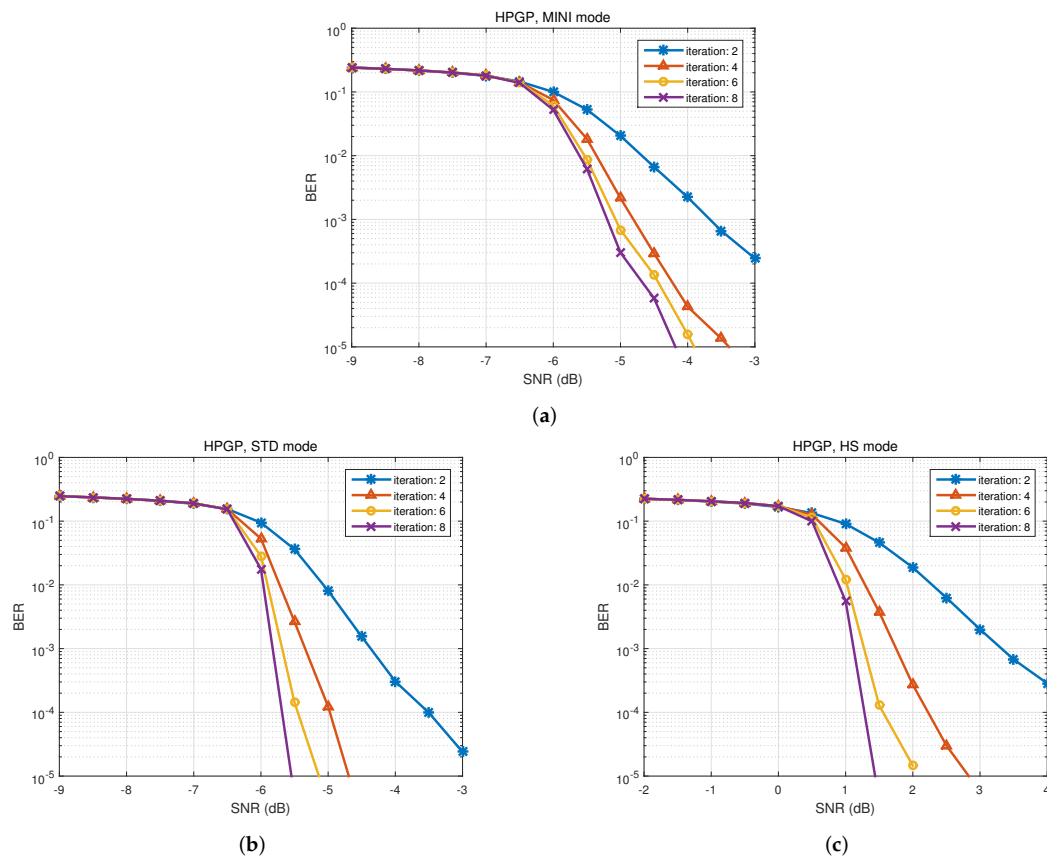


Figure 18. BER results for HPGP: (a) MINI mode; (b) STD mode; and (c) HS mode.

The BER results for HS PLC are shown in Figure 19. For the performance evaluation of HS PLC, the best and worst modes in terms of the BER are considered. The FEC in HS PLC does not use iterative decoding. Figure 19a shows the BER results for the NORMAL mode. An error floor is present and the BER does not fall below 0.02 in the NORMAL mode. There is no diversity in the NORMAL mode. In the DV mode, the BER decreases as the SNR increases due to the high diversity of 12 at the expense of the transmission rate, but the falling slope of the BER is not as rapid as that of IoT PLC or HPGP, which uses CTC for FEC.

In Figure 20, the BER performance of HS PLC and HPGP are shown for comparison. The STD mode of HPGP has the best performance at $\text{BER} = 10^{-3}$, followed by the MINI mode, the DV mode of HS PLC, and the HS mode of HPGP. In terms of the BER, the NORMAL mode of HS PLC shows the worst performance. The BER curves of HPGP are steeper than those of HS PLC. Thus, the difference between the BER values of the MINI mode of HPGP and the DV mode of HS PLC becomes larger as the SNR increases.

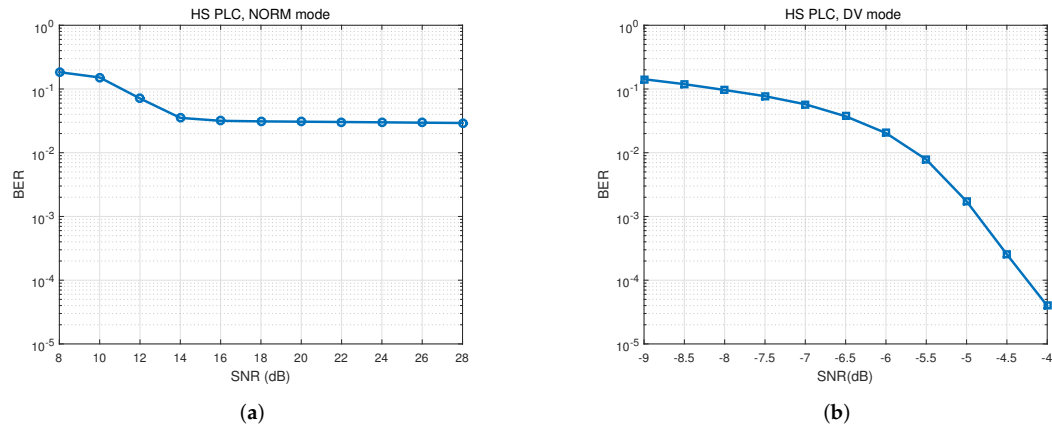


Figure 19. BER results for HS PLC: (a) NORMAL mode; and (b) DV mode.

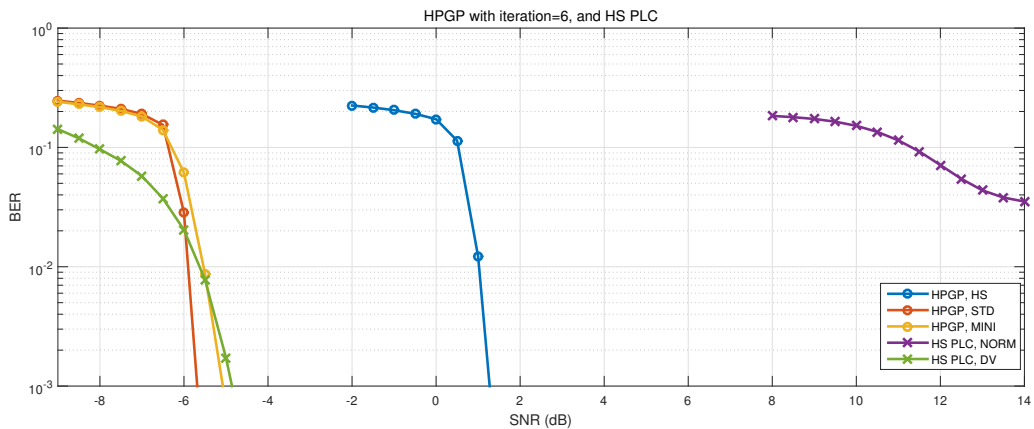


Figure 20. BER results of HPGP and HS PLC.

Now, performance comparisons of the three PLC technologies are provided. Since there are many modes of PLC technologies to compare, a plot would be very complex and difficult to read if all the BER curves for all the modes were shown in the same plot. Instead of comparing all the BER curves, the SNR value required to obtain a target BER at each mode of the PLC is compared. In Figure 21, the SNR values required to obtain a BER of 10^{-3} are shown for all modes of the PLC technologies. The horizontal axis is the diversity number (the number of copies for the coded bits) and the vertical axis represents the required SNR. Therefore, a lower point means better BER performance. The three dotted lines represent the results for IoT PLC. IoT PLC in QPSK mode has better BER performance than any other PLC technologies at each diversity number. The QPSK mode of IoT PLC with $DV_n = 15$ is the best in terms of the BER performance. The Mini DF of IoT PLC has an SNR value similar to the QPSK mode with $DV_n = 11$, but this SNR value cannot be achieved with the other PLC technologies.

On the other hand, the STD mode of HPGP outperforms the other two modes of HPGP and provides similar performance to the QPSK mode of IoT PLC with $DV_n = 4$. The HS mode of HPGP has a slightly worse performance than the QPSK mode of IoT PLC with $DV_n = 2$. The DV mode of HS PLC has worse performance than $\pi/4$ -DQPSK mode with $DV_n = 12$ and has similar performance to $\pi/4$ -DQPSK mode with $DV_n = 9$. The performance of the DV mode of HS PLC is worse than that of the STD and MINI mode of HPGP. However, the DV mode of HS PLC has better performance than the HS mode of HPGP. The NORMAL mode of HS PLC does not appear in this figure since it cannot achieve a BER of 10^{-3} on the PLC channel. This also applies to the 16QAM mode of IoT PLC with $DV_n = 1$.

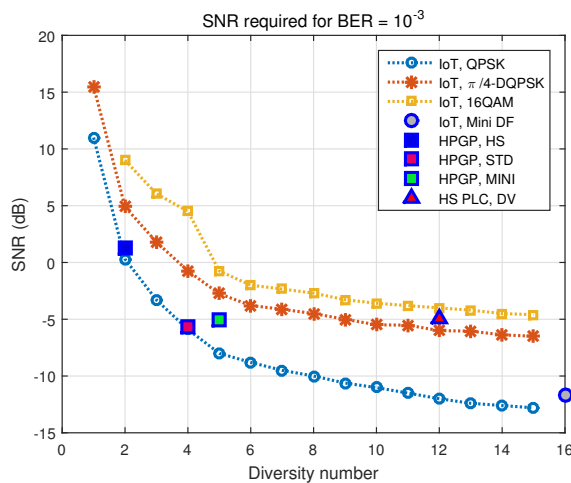


Figure 21. Comparisons of SNR required for BER of 10^{-3} .

5. Conclusions

This study compared the physical layer performance of broadband PLC technologies being deployed or tested in Korea. The PLC technologies included IoT PLC, HPGP, and HS PLC. The bit rate, power spectrum, and BER were evaluated. For the transmission rate, an expression for the bit rate for IoT PLC and HPGP was derived while taking the padding bits and the number of tones in use into consideration. The expression was compared with an approximate formula. IoT PLC provides 31 different bit rates ranging from 0.930 to 25.568 Mbps. HPGP and HS PLC each provides three different bit rates. The power spectrum was obtained through computer simulations. IoT PLC was found to have good power spectrum properties in terms of the notch depth and out-of-band power. For the BER performance comparisons, the upper bound of the BER for each PLC standard was evaluated through computer simulations. From the results, the STD mode of HPGP provides similar performance to the QPSK mode of IoT PLC with a diversity number of 4. Finally, we observed that IoT PLC in QPSK mode has better BER performance than any other PLC technologies at each diversity number.

Funding: This research was supported by a grant from the Korea Energy Efficiency Cooperative.

Conflicts of Interest: The authors declare no conflict of interest. The funders had no role in the design of the study; in the collection, analyses, or interpretation of data; in the writing of the manuscript, or in the decision to publish the results.

References

- Mohassel, R.R.; Fung, A.; Mohammadi, F.; Raahemifar, K. A survey on advanced metering infrastructure. *Electr. Power Energy Syst.* **2014**, *63*, 473–484. [[CrossRef](#)]
- Kim, D.S.; Chung, B.J.; Chung, Y.M. Statistical learning for service quality estimation in broadband PLC AMI. *Energies* **2019**, *12*, 684. [[CrossRef](#)]
- Uribe-Pérez, N.; Angulo, I.; de la Vega, D.; Arzuaga, T.; Fernández, I.; Arrinda, A. Smart grid applications for a practical implementation of IP over narrowband power line communications. *Energies* **2017**, *10*, 1782. [[CrossRef](#)]
- Chung, Y.M. Overview and characteristics of IoT PLC physical layer. In Proceedings of the International Conference of Electronics, Information, and Communication (ICEIC) 2020, Barcelona, Spain, 19–22 January 2020; pp. 99–101.
- Llano, A.; Angulo, I.; de la Vega, D.; Marron, L. Impact of channel disturbances on current narrowband power line communications and lessons to be learnt for the future technologies. *IEEE Access* **2019**, *7*, 83797–83811. [[CrossRef](#)]
- International Organization for Standardization. *Information Technology-Telecommunications and Information Exchange between Systems-Powerline Communication (PLC) Medium Access Control (MAC) and Physical Layer*

- (PHY)-Part 1: General Requirements; ISO/IEC 12139-1; International Organization for Standardization: Geneva, Switzerland, 2009.
- 7. HomePlug Alliance. HomePlug Green PHY Specification Release Version 1.1.1; HomePlug Alliance: Beaverton, OR, USA, 2013.
 - 8. Korea Smart Grid Association (KSGA). Smart Grid Technology Trends Report; KSGA: Seoul, Korea, 2012.
 - 9. Korea Electrical Manufacturers Association (KOEMA). General Requirements for Power-Line Communication (PLC) Media Access Control (MAC) and Physical Layer (PHY) for Internet of Things; SPS-KOEMA 0915-XXXX, submitted for Alliance Standards; Korea Electrical Manufacturers Association (KOEMA): Seoul, Korea, 2018.
 - 10. Gotz, M.; Rapp, M.; Dostert, K. Power line channel characteristics and their effect on communication system design. *IEEE Commun. Mag.* **2004**, *42*, 78–86. [[CrossRef](#)]
 - 11. Esmailian, T.; Kschischang, F.R.; Gulak, P.G. In-building power lines as high-speed communication channels: channel characterization and a test channel ensemble. *Int. J. Commun. Syst.* **2003**, *16*, 381–400. [[CrossRef](#)]
 - 12. Banwell, T.; Galli, S. A novel approach to the modeling of the indoor power line channel part I: Circuit analysis and companion model. *IEEE Trans. Power Deliv.* **2005**, *20*, 655–663. [[CrossRef](#)]
 - 13. Galli, S.; Banwell, T. A novel approach to the modeling of the indoor power line channel-part II: Transfer function and its properties. *IEEE Trans. Power Deliv.* **2005**, *20*, 1869–1878. [[CrossRef](#)]
 - 14. Canete, F.J.; Cortés, J.A.; Díez, L.; Entrambasaguas, J.T. A channel model proposal for indoor power line communications. *IEEE Commun. Mag.* **2011**, *49*, 166–174. [[CrossRef](#)]
 - 15. Tonello, A.M.; Versolatto, F. Bottom-up statistical PLC channel modeling-part I: random topology model and efficient transfer function computation. *IEEE Trans. Power Deliv.* **2011**, *26*, 891–898. [[CrossRef](#)]
 - 16. Tonello, A.M.; Versolatto, F. Bottom-up statistical PLC channel modeling-part II: Inferring the statistics. *IEEE Trans. Power Deliv.* **2010**, *25*, 2356–2363. [[CrossRef](#)]
 - 17. Marrocco, G.; Statovci, D.; Trautmann, S. A PLC broadband channel simulator for indoor communications. In Proceedings of the 2013 IEEE 17th International Symposium on Power Line Communications and Its Applications, Johannesburg, South Africa, 24–27 March 2013; pp. 321–326.
 - 18. Zimmermann, M.; Dostert, K. A multipath model for the powerline channel. *IEEE Trans. Commun.* **2002**, *50*, 553–559. [[CrossRef](#)]
 - 19. Hirayama, Y.; Okada, H.; Yamazato, T.; Katayama, M. Noise analysis on wide-band PLC with high sampling rate and long observation time. In Proceedings of the 7th International Symposium on Power-Line Communications and Its Applications, Kyoto, Japan, 26–28 March 2003; pp. 142–147.
 - 20. Andreadou, N.; Pavlidou, F. PLC channel: impulsive noise modelling and its performance evaluation under different array coding schemes. *IEEE Trans. Power Deliv.* **2009**, *24*, 585–595. [[CrossRef](#)]
 - 21. Meng, H.; Guan, Y.L.; Chen, S. Modeling and analysis of noise effects on broadband power-line communications. *IEEE Trans. Power Deliv.* **2005**, *20*, 630–637. [[CrossRef](#)]
 - 22. Andreadou, N.; Pavlidou, F. Modeling the noise on the OFDM power-line communications system. *IEEE Trans. Power Deliv.* **2010**, *25*, 150–157. [[CrossRef](#)]
 - 23. Mlynek, P.; Koutny, M.; Misurec, J. Power line modelling for creating PLC communication system. *Int. J. Commun.* **2010**, *4*, 13–21.
 - 24. Llano, A.; Angulo, I.; Angueira, P.; Arzuaga, T.; de la Vega, D. Analysis of the channel influence to power line communications based on ITU-T G.9904 (PRIME). *Energies* **2016**, *9*, 39. [[CrossRef](#)]
 - 25. Sanz A.; Sancho, D.; Guemes, C.; Cortés, J.A. A physical layer model for G3-PLC networks simulation. In Proceedings of the 2017 IEEE International Symposium on Power Line Communications and its Applications (ISPLC), Madrid, Spain, 3–5 April 2017; pp. 1–6.
 - 26. Hoch, M. Comparison of PLC G3 and PRIME. In Proceedings of the 2011 IEEE International Symposium on Power Line Communications and Its Applications, Udine, Italy, 3–6 April 2011; pp. 165–169.
 - 27. Matanza, J.; Alexandres, S.; Rodriguez-Morcillo, C. Performance evaluation of two narrowband PLC systems: PRIME and G3. *Comput. Stand. Interfaces* **2013**, *36*, 198–208. [[CrossRef](#)]
 - 28. Upadhyay, A.; Gupta, A.; Kumar, V. Comparative study of narrow band PLCs physical layer under AWGN and narrowband interferer. In Proceedings of the 2015 Annual IEEE India Conference (INDICON), New Delhi, India, 17–20 December 2015; pp. 1–4.
 - 29. IEEE Computer Society and the IEEE Microwave Theory and Techniques Society. In *IEEE Standard for WirelessMAN-Advanced Air Interface for Broadband Wireless Access Systems*; IEEE Std 802.16.1-2012; IEEE Standard Association: New York, NY, USA, 2012.

30. Ma, H.; Wolf, J. On tail biting convolutional codes. *IEEE Trans. Commun.* **1986**, *34*, 104–111. [[CrossRef](#)]
31. Kang, J.H.; Stark, W.E.; Hero, A.O. Turbo codes for fading and burst channels. In Proceedings of the 1998 IEEE Globecom, Communications Theory Mini Conference, Sydney, Australia, 8–12 November 1998; pp. 40–45.
32. Hall, E.K.; Wilson, S.G. Design and analysis of turbo codes on Rayleigh fading channels. *IEEE J. Sel. Areas Commun.* **1998**, *16*, 160–174. [[CrossRef](#)]
33. Welch, P. The use of fast Fourier transform for the estimation of power spectra: A method based on time averaging over short, modified periodograms. *IEEE Trans. Audio Electroacoust.* **1967**, *15*, 70–73. [[CrossRef](#)]
34. Sure, P.; Bhuma, C.M. A survey on OFDM channel estimation techniques based on denoising strategies. *Eng. Sci. Technol. Int. J.* **2017**, *20*, 629–636. [[CrossRef](#)]
35. Lin, C.-H.; Chen, C.-Y.; Wu, A.-Y.; Tsai, T.-H. Low-power memory-reduced traceback MAP decoding for double-binary convolutional turbo decoder. *IEEE Trans. Circ. Syst. Regul. Pap.* **2009**, *56*, 1005–1016.
36. Kim, J.H.; Park, I.-C. Double-binary circular turbo decoding based on border metric encoding. *IEEE Trans. Circ. Syst.-II Exp. Briefs* **2008**, *55*, 79–83. [[CrossRef](#)]
37. Claussen, H.; Karimi, H.R.; Mulgre, B. Improved max-log-MAP turbo decoding by maximization of mutual information transfer. *EURASIP J. Adv. Signal Process.* **2005**, *2005*, 820–827. [[CrossRef](#)]



© 2020 by the author. Licensee MDPI, Basel, Switzerland. This article is an open access article distributed under the terms and conditions of the Creative Commons Attribution (CC BY) license (<http://creativecommons.org/licenses/by/4.0/>).